MIT Libraries | DSpace@MIT

MIT Open Access Articles

Finite Element Simulation of Hot Nanoindentation in Vacuum

The MIT Faculty has made this article openly available. ***Please share*** how this access benefits you. Your story matters.

Citation: Lee, H., Y. Chen, A. Claisse, and C.A. Schuh. "Finite Element Simulation of Hot Nanoindentation in Vacuum." Experimental Mechanics 53, no. 7 (February 5, 2013): 1201–1211.

As Published: http://dx.doi.org/10.1007/s11340-012-9700-7

Publisher: Springer US

Persistent URL: http://hdl.handle.net/1721.1/103335

Version: Author's final manuscript: final author's manuscript post peer review, without publisher's formatting or copy editing

Terms of use: Creative Commons Attribution-Noncommercial-Share Alike

Massachusetts Institute of Technology

Finite element simulation of hot nanoindentation in vacuum

Hunkee Lee[1], Ying Chen[1,2], Antoine Claisse[1], Christopher A. Schuh[1*]

[1] *Department of Materials Science and Engineering, Massachusetts Institute of Technology, 77 Massachusetts Avenue, Cambridge, MA 02139, USA*

[2] *Department of Materials Science and Engineering, Rensselaer Polytechnic Institute, 110 8th Street, Troy, NY 12180, USA*

Abstract

A finite element model is developed to investigate technical issues associated with hot nanoindentation measurements in vacuum, e.g. thermal expansion-induced drift and temperature variations at the contact region between the cold indenter tip and hot specimen. With heat conduction properly accounted for, the model is able to reasonably reproduce experimental indentation measurements on fused silica and copper—two materials with significantly different thermal and mechanical properties—at several temperatures. Temperature and loading rate effects on thermal drift are established using this model and an analytical expression for predicting thermal drift is numerically calibrated. The model also captures details of the indentation process that are not directly accessible experimentally, and reaffirms the need for operational refinements in order to acquire high temperature indentation data of high quality, especially in a vacuum environment. Such information can guide experiments aimed at understanding thermally-activated phenomena in materials.

Keywords; FEM, high temperature nanoindentation, thermal drift, nanomechanical properties measurement

---

[*] Corresponding author. *Email address:* schuh@mit.edu (C.A. Schuh).

Introduction

Nanoindentation at elevated temperatures has been attracting growing interest in recent years, not only as a means to measure the mechanical properties (e.g., modulus and hardness) of small structures at practical service temperatures [1~9], but also because it is capable of probing high temperature deformation mechanisms on the nanoscale [10~21]. As the indentation depth normally ranges only from dozens to hundreds of nanometers, the material volume probed by nanoindentation is very small. As a result, internal dynamic events such as dislocation motion [22~24], shear banding [25,26], and phase transformation [27~29] can result in evident discontinuities on the measured load P-displacement h curve. At high temperatures, however, the capability of extracting mechanical properties or inferring atomic scale structural changes under stress from the P-h curve is affected by thermal drift.

It is a major technical challenge to identify the origin and extent of thermal drift for a specific high-temperature nanoindentation apparatus and experiment, and to further control or minimize its effect during high temperature nanoindentation. There are several thermally-related factors that could cause drift, including thermal effects on electric systems, fluctuation of temperature in the specimen, heat convection from the heating source and specimen to the environment, and heat conduction between the specimen and the indenter tip when the two are brought into contact. Among these factors, heat conduction tends to trigger the most displacement drift for high temperature nanoindentation in a vacuum environment, as it leads to rapid development of temperature gradients and thermal strain that superimposes onto the true response of the specimen. In other words, the “indentation displacement” measured by the transducer is in general different from the actual indentation depth at the indenter tip, and the difference between them is the change in the height of the tip assembly caused by the thermal strain (as well as inevitable mechanical strain).

Thermal drift is commonly revealed by the net displacement under fixed load for a brief period (several seconds), either at a small fixed pre-load (e.g., 2 μN) or during unloading when the load is held at a small fraction (e.g., 20%) of the peak load [11]. The average preload drift rate is rather small, i.e., 0.1-0.25 nm/s, and is almost independent of the temperature and only very weakly dependent upon materials properties such as the thermal conductivity and hardness of the specimen. On the contrary, the unload drift rate is many times larger, and increases considerably with temperature, the thermal conductivity of the specimen, and the contact area (which is inversely proportional to specimen hardness); for example, it increases from about 0.2 nm/s at room temperature to 1.7 nm/s at 773 K for fused silica, and for copper, which has a much higher thermal conductivity, it can reach as high as about 37 nm/s at 590 K [11].

Considering the extremely high thermal conductivity, ~2400 W/mK [30], of the diamond indenter tip, it has been proposed that the tip can rapidly achieve thermal equilibrium with the specimen upon contact and therefore the tip itself does not contribute substantially to the observed drift [10,11]. Instead, the rest of the tip assembly experiences much more gradual temperature rise and more significant expansion, due to its relatively lower thermal conductivity and larger dimensions. Trenkle et al. [11] proposed a one-dimensional heat flow model where a cold semi-infinite shaft comes into contact with a hot semi-infinite specimen at time $t = 0$, and derived an equation for the thermal drift as a function of time in terms of the thermal properties of the specimen and shaft. The model is able to capture some general trends observed experimentally, i.e., an increase in thermal drift with temperature, contact area, and the thermal conductivity of the specimen, although its predictions do not exactly match the measured drift rate due to its static nature and the simplified geometry used. Everitt et al. [31] considered the same static heat conduction problem, but incorporated the axisymmetric, three-dimensional geometry of the tip assembly and sample, with the tip positioned at 1 μm indentation depth. With the bottom of the specimen and the top of the tip holder held at a fixed high and low temperature, respectively, they solved for the temperature evolution of the two after contact by the finite element method. This model confirmed that the specimen temperature and thermal conductivity significantly affect the temperature distribution in the system (and therefore the overall thermal drift). However, both of the models described above only considered thermal conduction between two still objects, and did not address the mechanical and dynamic aspects of hot indentation.

Here, we carry out a finite element analysis of the hot nanoindentation process, which allows us to monitor the temperature evolution and the deformation behavior of the system during indentations conducted in a vacuum. We perform indentation simulations on specimens with different thermal conductivities, and at several temperatures ranging from room temperature up to 673 K and at several loading rates as well. At each temperature and loading condition, we compare the actual vs. apparent tip penetration depth, and thereby assess the thermal drift over the entire indentation process. The simulation results are compared with prior experimental measurements [11], and provide insights regarding the use of high temperature nanoindentation experiments to study thermally-activated materials phenomena and temperature-dependent materials properties.

Finite element model

Our model indentation system is shown schematically in Fig. 1(a). The tip assembly consists of a macor shaft and a diamond indenter tip that are joined together by a layer of titanium-based brazing alloy. The arrangement and dimension of each of these components are set to simulate the nanoindenter platform from Hysitron Inc. (Minneapolis, MN), which our group has used extensively to perform hot nanoindentation experiments on a variety of materials [10~12,16,18,19,21,24,25]. As a result, we are able to compare our simulation results later with some load-displacement (*P*-*h*) curves and thermal drifts measured by this specific indenter. We specifically model the case of vacuum indentation, where there is no convective atmosphere.

The indenter assembly shaft is 8 mm in height, which is about 133 times the total height of the diamond tip and brazing layer, and therefore even slight temperature excursion and thermal strain in the shaft can cause substantial elongation. Connected to the shaft by a brazing layer is an axisymmetric conical indenter of semi-apical angle 70.3º, which yields a projected area equivalent to that of the Berkovich tip [32,33]. The indenter tip is taken to be blunt, with a radius of 200 nm. The overall height of the tip is 20 μm, while the thickness of the specimen is 40 μm.

The high temperature indentation process is simulated using the commercial finite element software ABAQUS/Standard. All parts in the model are meshed with axisymmetric 4-node bilinear elements CAX4T that allow for coupled temperature-displacement analysis. The element sizes are extremely small, e.g., as small as 0.05 nm, near the contact, and gradually increase to about 120 μm far away from the contact. A close-up of the mesh in the shaft, tip and specimen is shown in Fig. 1(b). Overall, the entire tip assembly is modeled with about 17800 elements and the specimen with about 8700 elements.

Table 1 summarizes the mechanical and thermal properties of all materials used in this work, including the elastic modulus, Poisson’s ratio, yield stress, thermal conductivity, density, thermal expansion coefficient, and specific heat capacity. The macor shaft and titanium-based braze are assumed to deform only elastically during the entire indentation process, as the stress level in them is very low due to their large cross-sectional areas. We assume that the diamond tip also only deforms elastically during indentation, but we take into account the linear temperature dependence of its elastic modulus.

Indentation simulations are performed on both fused silica and pure copper; as copper is much softer and more thermally conductive than fused silica, a different thermal response is anticipated. The mechanical properties of the fused silica and copper are described by an elastic plus power-law work hardening relationship, which in one-dimensional form reads:

$$\boldsymbol{\sigma} = \begin{cases} \boldsymbol{E\varepsilon} & (0 \le \boldsymbol{\varepsilon} \le \boldsymbol{\varepsilon}_y) \\ \boldsymbol{\sigma}_y + \boldsymbol{F}(\boldsymbol{\varepsilon} - \boldsymbol{\varepsilon}_y)^n & (\boldsymbol{\varepsilon}_y \le \boldsymbol{\varepsilon}) \end{cases} \tag{1}$$

where σ is stress, σ_y is the yield stress, E is elastic modulus, Ɛ is strain, F is the strength coefficient, and n is the work hardening exponent. The elastic modulus and yield stress of both materials as a function of temperature, as listed in Table 1, are deduced from prior high temperature nanoindentation measurements (a Tabor factor of 1.5 for fused silica [36] and 3.0 for copper [37] are used respectively to determine the yield stress). Fused silica is taken to be elastic-perfectly plastic (F=0) [34], while copper undergoes work hardening beyond yield (its temperature-dependent F and n values are obtained from prior tensile tests and are given in Table 1) [35]. We also use temperature-dependent thermal conductivities for both materials. Rate-dependent and creep behaviors are explicitly neglected in this study, which is reasonable for the range of rates, temperatures and stresses we focus on.

The interaction between the indenter tip and the top surface of the specimen is defined as a “hard” contact (when the two surfaces are separate, there is no pressure; when they are in contact, any pressure can be transferred between them) in the normal direction, while frictionless sliding is allowed in the tangential direction. Heat can only be transferred across the contact by conduction, and the contact thermal conductance is assumed infinite when the two surfaces are in contact. Contact conditions are enforced between the top of the specimen (master surface) and the bottom of the tip (slave surface) by surface-to-surface discretization with finite sliding, which takes into account the local shape of both surfaces near contact and thus provides relatively reliable stress solutions.

In our model, heat transfer takes place solely by conduction, which is reasonable for indentations conducted in vacuum as done experimentally in Ref. [11]. The bottom of the specimen is held at a fixed set temperature throughout the indentation process. Prior to applying any load, a thermal equilibration step is carried out so that the temperature in the entire specimen reaches the set temperature. The entire tip assembly including the shaft, braze, and tip, assumes an initial temperature of 293 K, and the temperature at the top of the shaft is kept at 293 K during indentation**.** The bottom of the specimen is constrained in the loading direction, while uniform compressive stress is applied at the top of the shaft to simulate the indentation process. In order to compare with prior experimental results [11], the same loading function is used as shown in Fig. 2. The maximum load P_{max} we use is 9.5 mN for fused silica and 3.0 mN for copper. We conduct a thermal-mechanical analysis of the entire indentation process at several load ramping rates, including 1, 4, and 8 mN/s, and at multiple temperatures up to 673 K.

Comparison to Experiments

The number of published experimental works that conform to the conditions of the present simulations is relatively small (especially due to our focus on vacuum indentation), and so we first examine the ability of the model to reproduce the key experimental signatures. Later, we turn to details revealed by the model which are not accessible directly by experiments.

We first run an indentation simulation on fused silica at 593 K with a loading rate of 4 mN/s, and compare the simulations with prior experimental results [11] acquired in vacuum under the same loading conditions in Fig. 3. The displacements from simulations reported in Fig. 3 are those at the top of the shaft, as the displacements from experiments are measured by a transducer located above the tip assembly. Fig. 3(a) shows the load-displacement curves from simulation and experiment as solid and dashed lines, respectively. The tip assembly expands during preload holding, so as is done in experimental reporting, the displacement at the end of preload segment is assigned a value of zero. The simulation and experimental results in Fig. 3(a) generally agree with each other very well. The unload drift (the net displacement accumulated during the unload holding) from Fig. 3(a) is further plotted as a function of the holding time in Fig. 3(b), where simulation results are plotted as the solid line while experimental data are plotted as open squares. The simulation results yield a linear slope of 1.25 nm/s, which is the average drift rate and agrees with that of the experimental data. Thus the model is capable of capturing the rate of heat conduction in experiments; as the load is held constant during this period, the elastic strain in the entire tip assembly remains constant and therefore the change in shaft dimension is solely due to thermal expansion.

We further run simulations on fused silica at 593 K but at different loading rates of 1 and 8 mN/s, and present the results in Fig. 3(b) as a dotted line and a dashed line, respectively. The total unload drift for a 10 s hold is 8.8 nm at loading rate of 1 mN/s, 12.5 nm at 4 mN/s, and 12.9 nm at 8 mN/s; thermal drift is significantly smaller at 1 mN/s than at 4 or 8 mN/s. This is because there is already sufficient time for heat transfer at the slow loading/unloading rate of 1 mN/s prior to the unload holding. Therefore the loading rate can affect the unload drift and drift rate during indentation on fused silica at 593 K.

We next consider additional indentation simulations at several different specimen temperatures using a loading rate of 4 mN/s. The average unload drift rates $\dot{U}$ determined from these simulations are plotted as a function of set temperature for fused silica and copper in Fig. 4(a) and 4(b), respectively. They are largely in line with available experimental results [11], which are included in Fig. 4 as hollow data points. At each temperature above ambient temperature, $\dot{U}$ for copper is over a dozen times larger than $\dot{U}$ for fused silica. For both fused silica and copper, $\dot{U}$ increases with specimen temperature. Higher specimen temperature leads to a steeper temperature gradient and faster heat conduction across the contact, and consequently greater thermal expansion of the shaft. The drift rate seems to follow a nearly linear dependence on the temperature, and a simple linear fit yields a slope of $d\dot{U}/dT$ = 0.0043 nm/s·K for fused silica and 0.1198 nm/s·K for copper. The difference in the $d\dot{U}/dT$ values between fused silica and copper reflects their drastically different thermal conductivity, and possibly their very different hardness values as well, since hardness affects the contact area available for heat exchange between tip and sample. This will be discussed in more detail later in the discussion section.

Unmeasured Details

With confirmation that the present model can reproduce the experimentally-measured output of hot indentation experiments on copper and fused silica, we now provide a more detailed view of effects that contribute to the measured results, but which are not themselves directly observed in the published experiments. We begin with a detailed examination of the displacement history during an indentation.

During indentation experiments, the displacement measured by the transducer is that at the top of the tip assembly. The displacement at the indenter tip, which is the true indentation depth, is not known and cannot be easily deduced when the tip assembly not only undergoes elastic deformation but also experiences nonuniform thermal expansion. This problem for high temperature nanoindentation might be mitigated by performing indentation tests at very high rates, so that there is little time for heat conduction to occur. However, even so, the discrepancy between the measured displacement and the actual indentation depth might not be able to be completely eliminated. Also, more often than not low loading rates are desired, particularly when the properties of materials under investigation are rate-dependent. Finite element modeling of the kind done here can shed light on this issue, as it can keep track of the tip displacement throughout the indentation process.

We now compare the displacement at the top of the shaft, U_{shaft}, to that at the bottom of the indenter tip, U_{tip}, during indentation at three different loading rates, 1, 4, and 8 mN/s. As rate and temperature effects are coupled in this problem, we further study the rate effect at two different temperatures, 473 and 673 K. The load-displacement curves from these simulations are assembled in Fig. 5(a) and (c) for fused silica and in Fig. 5(b) and (d) for copper. In these figures, P-U_{shaft} curves are plotted as lines while P-U_{tip} curves are plotted as open symbols; downward displacement is deemed positive and upward negative. For each material and at each temperature, the P-U_{tip} curves from the three different rates completely overlap each other. This is expected since U_{tip} is the true indentation depth and is determined by the applied load, because in this study the material properties are assumed to be independent of rate. In contrast, the behavior of U_{shaft} is much more complex and exhibits rate dependence as will be discussed below.

During indentation the tip assembly also experiences compressive elastic strain, which is proportional to the applied load. The elastic mechanical strain in the shaft is very small (e.g., it is only about 1.6 x 10^{-7} at a load of 9.5 mN in the absence of thermal effects, and corresponds to a shrinkage of about 1.3 nm in shaft height). In contrast, the compressive strain in the indenter tip is much larger in magnitude (although diamond is much harder than macor), due to the much smaller cross-sectional area in this region. For example, in a mechanical calculation with no thermal effects, at a load of 9.5 mN the elastic strain ranges from 4.4 x 10^{-5} at the top of the diamond tip to 9.5 x 10^{-3} at its bottom; the height of the diamond tip decreases by 12.3 nm. Such compressive strain alone could cause an increase in the downward displacement at the shaft top. Therefore when thermal expansion is trivial, as is the case for indenting fused silica at 473 K, U_{shaft} would be larger than U_{tip} due to this mechanical effect, as shown in Fig. 5(a). The difference between them is about 11 nm at the peak load for the 8 mN/s case, and is comparable to the decrease in the height of the diamond tip discussed above. This purely mechanical effect would superimpose upon the normal machine compliance, which is routinely accounted for in experimental studies through calibration.

At lower loading rates or higher specimen temperatures, the shaft experiences greater thermal expansion, which drives the shaft top to move up more with respect to its bottom under load control. Therefore U_{shaft}, the net downward displacement of the shaft top, becomes smaller and the P-U_{shaft} curves shift to the left in Fig. 5. For example, as shown in Fig. 5(c), as we decrease the loading rate to 1 mN/s and increase the temperature from 473 to 673 K when indenting fused silica, U_{shaft} is now no longer larger than U_{tip} and becomes much smaller than U_{tip} during unloading. When the specimen is copper (which has a much larger thermal conductivity than fused silica),

U_{shaft} is always much smaller than U_{tip} due to significant thermal expansion, as shown in Fig. 5(b) and (d). At 673 K, the shaft has expanded so much that eventually U_{shaft} becomes negative, i.e., the final position of the top of the shaft at the end of unloading is much higher than its initial position prior to loading. The rate dependence of U_{shaft} shown here also calls for caution when nanoindentation is used to probe the rate effects of materials at high temperatures.

Consistent with prior observations made in connection with Fig. 3(b), loading rate dependency of the total unload drift measured during unload holding is also found in copper, and to a much more significant degree. In the case of copper at 673 K, which exhibits the largest unload drift in this study, the maximum difference in unload drift is about 100 nm across the range of studied rates (unload drift is 378 nm at loading rate of 1 mN/s and 471 nm at 8 mN/s). The contact time between tip and specimen is longer as loading rate decreases, so the temperature rise in the shaft prior to unload holding is more developed. The corresponding U_{shaft} curves due to loading rate are also in line with this drift dependency. U_{shaft} becomes smaller as loading rate decreases and in the case of copper at 1 mN/s and 673 K, the slope of the loading curve near the peak load is no longer even positive, and the unloading curve unphysically crosses the loading curve.

The drastic differences between the thermal responses when indenting fused silica and copper can be more easily appreciated by comparing the temperature distribution in the system. Fig. 6 shows the transient temperature along the axisymmetric axis (i.e., at $x = 0$) as a function of y, the distance in the loading direction, when indenting fused silica and copper at 673 K with a rate of 4 mN/s. The temperature distributions at four instants are shown: (1) at the end of preload holding, (2) at the peak load, (3) at the beginning of unload holding, and (4) at the end of unload holding. The temperature in the tip assembly is shown in Fig. 6(a) and (b) for the case of indenting fused silica and copper, respectively, and the horizontal axis in these figures is the distance above the bottom of the tip. In both cases, the tip assembly experiences similar histories of temperature change. During the preload period the tip end achieves thermal equilibrium with specimen and maintains equilibrium during the entire indentation process. This observation is in line with prior arguments that the near-contact region of a diamond tip should be able to attain equilibrium with a heated sample, especially since the preload hold in this study is one hour—equal to the thermal equilibration time reported experimentally [10] and used as a standard for preheat equilibration of the system in other subsequent studies [1,7,13,16,25].

After the indentation begins in earnest, the temperature in the shaft, behind the diamond tip, continues to rise during loading, unloading and unload holding. For example, the temperature at a point 500 μm above the tip end rises by about 1 K for the case of fused silica but much more than 20 K for the case of copper by the end of unload holding. For all four times shown in Fig. 6, temperature decreases with distance along the shaft, and eventually converge to 293 K at the top of the shaft (not shown in Fig. 6(a) and (b)). Since the temperature rise in the shaft is directly responsible for the drift displacement (and specifically, the temperature increase during unload holding accounts for the experimentally measured unload drift), these differences explain the drift results seen earlier in Fig. 4. We will discuss this in greater length in the section that follows.

Discussion

The above simulation results represent an important validation of proposals in the literature regarding drift and other thermal issues in hot nanoindentation, especially as regards the special case of indentation in vacuum. As discussed in detail in the experimental paper of Trenkle et al. [11], vacuum removes a major conduit of heat transfer between tip and sample, namely convective transport through the surrounding medium. As a result, the tip only experiences heating through a small conductive contact with the specimen, and this leads to various negative results anticipated by Trenkle et al. [11].

Specifically, the differences between actual and apparent indentation depth arise from thermal expansion of the tip assembly. There is little drift before the indentation begins, because the whole tip assembly becomes thermally stable during 1 hour of preload at 2 μN. However, upon indentation the contact area rises rapidly, as does heat transfer into the tip and concomitant thermal expansion. Drift during unload holding is especially problematic because of the large contact area of the residual impression. Trenkle et al. [11] described the thermal drift U as a function of holding time, temperature, materials properties, and contact area, based upon which we can write the average drift rate $\dot{U}$ during unload holding from $t = 0$ to t_0 here:

$$\boldsymbol{\dot{U}} = \boldsymbol{B} \cdot \frac{\boldsymbol{\alpha}_{shaft}}{\frac{1}{\sqrt{\boldsymbol{D}_{shaft}}} + \sqrt{\frac{\boldsymbol{A}_{shaft}}{\boldsymbol{D}_{specimen}\boldsymbol{A}_c}}} \cdot \frac{1}{\sqrt{\boldsymbol{t}_0}} \cdot [\boldsymbol{T}_{specimen} - \boldsymbol{T}_{shaft}^{t=0}] \tag{2}$$

where α_{shaft} is the thermal expansion coefficient of the shaft. The thermal diffusivity $D = k/(\rho C_p)$, with k being the thermal conductivity, ρ the density, and C_p the specific heat capacity. A_{shaft} is the cross-sectional area of the shaft. A_c is the contact area and is determined from $A_c = 24.5h^2$, where h is the true indentation depth (i.e., $h=U_{\mathrm{tip}}$). This equation was originally derived [11] based on sudden one-dimensional thermal contact between two semi-infinite bodies at different temperatures, and here we have replaced the original constant $2/\sqrt{\pi}$ with a scaling parameter B to account for the geometric and mechanical complications of the true indentation contact problem.

Equation (2) captures the linear dependence of the average drift rate $\dot{U}$ on T_{specimen}. With $T_{shaft}(t = 0) = 293$ K and $t_0 = 10$ s, we fit the data in Fig. 4 that plots $\dot{U}$ as a function of T_{specimen} to Equation (2), and obtain $B = 2.94$ for fused silica and $B = 4.27$ for copper respectively; these fitting results are plotted as solid lines in Fig. 4. These lines appear slightly non-linear because the contact area A_c in Equation (2) is not a constant but rather is dependent upon temperature as a result of the temperature-dependent mechanical properties used in the model. The fitted values for the constant B for the two materials are reasonably close together, and in fact it may be convenient to use a single value of B that reasonably represents both. Best fitting of both data sets together yields $B = 3.38$, which as shown in Fig. 4 with dotted lines slightly overestimates the drift in fused silica, and slightly underestimates it in copper. In any event, the fitted values of B are significantly higher than the constant emerging from the model of Trenkle et al., B = $2/\sqrt{\pi}$ [11], the predictions of which are also included in Fig. 4 as dashed lines; the difference is about a factor of three, which is a reflection of the added dimensions for heat transfer in the 3D model, and the superposition of heat flow along them. Equation (2) also explicitly shows that $\dot{U}$ increases with α_{shaft}, D_{shaft}, D_{specimen}, and A_c, but decreases with larger A_{shaft} and longer holding time t_0.

As $\sqrt{A_{shaft}/(D_{specimen}A_c)}$ is on the order of 10^6 $\text{s}^{-1/2}\text{m}^{-1}$ and 10^5 $\text{s}^{-1/2}\text{m}^{-1}$ when the specimen is fused silica and copper, respectively, it is several orders of magnitude higher than $1/\sqrt{D_{shaft}}$ which is only about 1168 $\text{s}^{-1/2}\text{m}^{-1}$. Therefore to a reasonable approximation, Equation (2) may be simplified as:

$$\begin{aligned}\dot{\boldsymbol{U}} &= \boldsymbol{B}\cdot\frac{\boldsymbol{\alpha}_{\boldsymbol{shaft}}\sqrt{\boldsymbol{D}_{\boldsymbol{specimen}}\boldsymbol{A}_{\boldsymbol{c}}}}{\sqrt{\boldsymbol{A}_{\boldsymbol{shaft}}\boldsymbol{t}_0}}\cdot[\boldsymbol{T}_{\boldsymbol{specimen}}-\boldsymbol{T}_{\boldsymbol{shaft}}^{\boldsymbol{t}=0}] \\ &\propto \boldsymbol{h}\sqrt{\boldsymbol{D}_{\boldsymbol{specimen}}}\end{aligned} \qquad (3)$$

Since $\sqrt{D_{Cu}}/\sqrt{D_{SiO2}} \approx 10.8$ and for the unload holding conditions, $h_{Cu}/h_{SiO2} \approx 1.8$, we obtain $\left(h_{Cu}\sqrt{D_{Cu}}\right)/\left(h_{SiO2}\sqrt{D_{SiO2}}\right) \approx 19.9$. This value is consistent with the ratio (which is ~ 21.7) between the average unload drift rates of copper and fused silica in all the present simulations at elevated temperatures (see Fig. 4).

It is very encouraging that the present, more sophisticated FEM model can reproduce the same trends noted by Trenkle et al. [11] both in their experimental data and in their simple analytical heat transfer analysis. Our conclusions therefore echo those of Trenkle et al., namely that exaggerated drift is a problem endemic to hot indentation if there is any scope for heat transfer into colder components in the load train. This is particularly so in a vacuum environment, where thermal equilibrium between tip assembly and specimen is difficult to establish. Trenkle et al. [11] proposed the use of a shaft material with very low or zero thermal expansion coefficient to reduce this effect, and showed significant improvements with such a tip assembly.

It is also of concern that in a vacuum indentation experiment the specimen temperature near the contact zone can be significantly different than the nominal setpoint. Because of the heat transfer from the hot specimen to the cold tip, the temperature in the specimen near contact is lower than the set point temperature desired. Fig. 6(c) and (d) show the temperature distribution in fused silica and copper at $x = 0$ beneath the contact when the set temperature is 673 K and the loading rate is 4 mN/s, and the horizontal axis is the distance below the initial top surface of the specimen. Since the actual specimen top surface is lower than its initial position during indentation, the data in Fig. 6(c) and (d) do not start at zero distance except for the curves representing the temperature at the end of preload. The specimen top already experiences temperature drop at the end of preload, and the drop is particularly pronounced in fused silica. At the peak load, the temperature at contact is only about 300 K in fused silica and is about 620 K in copper; even at distances as far as 2 μm below contact, the temperature is only about 540 K in fused silica and 650 K in copper.

To reveal the size of the affected zone, we further plot in Fig. 7(a) and (b) contours of temperature at the peak load in fused silica and copper, respectively. What is important to remember in this context is that Fig. 7 show only a cross-section of the full volume of interest in the test. When the temperature is volume-averaged over the plastic zone, the effect of near-contact cooling can be more properly assessed. As a first simple approach, we take the plastic zone as the hemispherical region within a radius of 1.9 times the contact half-length [46~48]. The plastic zone radius is about 1.4 μm for fused silica and 1.9 μm for copper. We compare the average plastic zone temperature with the setpoint temperature in Fig. 8.

The difference between the “true” plastic zone temperature and the setpoint is actually subtle in the case of copper, owing to the high thermal conductivity of the sample and its ability to “back-fill” heat lost to the tip. In the case of copper and high conductivity materials like it, we conclude that although there may be regions locally cooled near the contact, the true test temperature, when averaged over the plastic zone, can be considered close to the corresponding set temperature, with an error bar of order ~5 %.

In the case of a low conductivity material like fused silica the opposite situation seems to develop. Although the amount of drift resulting from heat transfer into the tip is lower (cf. Fig. 4), the low sample conductivity leads to significant thermal gradients in the sample near the contact (Figs. 6-8). For example, when the set temperature is 673 K, the calculated average temperature over the plastic zone is 402 K for fused silica (about 270 K difference). Fig. 8 suggests that over the range of test temperatures examined here, the error on the true test temperature is about -40 % for fused silica. It is hoped that in future work the present model could be used to design a test paradigm in which some indentations are used to first heat the shaft sufficiently that a subsequent indentation may accurately sample the intended sample temperature.

Other authors have proposed separate heating systems for tip and sample [13,20,49~51] and this approach should be given special attention for indentation in vacuum as a means of overcoming the exaggerated drift rates of Equation (2). In a gas atmosphere the experiments of Trenkle et al. [11] offer significant evidence that the tip is more evenly heated by its mere proximity to the hot sample, owing to increased convective transport of heat between sample and tip. A detailed numerical analysis including such effects remains to be conducted; this represents a key direction for future finite element modeling. The fact that such a model can faithfully reproduce results from a vacuum environment is regarded as an important first step towards eventually addressing such complex situations.

Conclusions

We have investigated high temperature nanoindentation testing using a finite element model with consideration of heat transfer, which offers insights on complexities that generally cannot be measured in experiments, including drift and the true penetration depth, and temperature gradients in the tip assembly and in the sample near the contact zone. The model is specifically relevant only to indentation in a vacuum, and the salient conclusions are listed below:

1. The proposed model is able to reproduce all of the available experimental observations on vacuum hot nanoindentation for two very different materials (copper and fused silica). The agreement with experiment is good in terms of load-displacement curves, thermal drift kinetics and temperature dependence. Heat conduction into the cold tip assembly from the hot specimen is the major factor inducing thermal drift for hot nanoindentation in a vacuum environment.

2. Under vacuum, the only heat transfer from sample to tip occurs via the mechanical contact point, and this leads to two undesirable effects. First, this causes exaggerated thermal drift that is a complex function of the test history, because the contact area changes as the sample is plastically deformed. We are able to track and analyze this complex drift for the first time with the proposed model. In a simplified setting, as during a constant-load holding period, the drift is more predictable, and here we use the modeling results to successfully calibrate the simple one-dimensional model of Trenkle et al. [11] to this situation. Second, heat transfer between the cold tip and hot specimen causes undesired specimen cooling near the contact region. This increases the error bar on the test temperature, only somewhat for a high conductivity material like copper (~5 %), but by a large amount (~40 %) in a low conductivity material like fused silica.
3. Our study supports proposals in the literature for improved high-temperature nanoindentaion testing, including, e.g., separate tip heating or operation in a gas atmosphere for thermal equilibrium between tip and specimen, and the use of a tip assembly with very low or zero thermal expansion coefficient to suppress artificial drift displacements.

Most of the materials phenomena that are studied by nanoidentation, including plasticity, phase transformation, shear localization, etc., are thermally activated phenomena. The use of high-temperature nanomechanical testing is therefore expected to rise in the coming years. The use of combined thermal and mechanical models such as the one proposed here can help to better deconvolve thermal and mechanical effects, to analyze and interpret experimental signals, and to design test paradigms appropriate to a given test material.

Acknowledgments

This work was supported by the US Army Research Office through the Institute for Solider Nanotechnologies at MIT. This work is also partially supported by the National Research Foundation of Korea Grand funded by the Korean Government (Ministry of Education, Science and Technology) [NRF-2010357-D00003]. The authors would like to thank Jonathan C. Trenkle for the experimental data and helpful discussion.

References

1. Smith JF, Zheng S (2000) High temperature nanoscale mechanical property measurements. Sur. Eng 16:143-146. doi: 10.1179/026708400101517044
2. Wolf B, Bambauer KO, Paufler P (2001) On the temperature dependence of the hardness of quasicrystals. Mater Sci Eng A 298:284-295. doi: 10.1016/S0921-5093(00)01287-9
3. Kramer DE, Yoder KB, Gerberich WW (2001) Surface constrained plasticity: Oxide rupture and the yield point process. Philos Mag A 81:2033-2058. doi: 10.1080/01418610108216651
4. Kraft O, Saxa D, Haag M, Wanner A (2001) The effect of temperature and strain rate on the hardness of Al and Al-based foams as measured by nanoindentation. Z Metallkd 92:1068-1073
5. Beake BD, Smith JF (2002) High-temperature nanoindentation testing of fused silica and other materials. Philos Mag A 82:2179-2186. doi: 10.1080/01418610210134387
6. Beake BD, Goodes SR, Smith JF (2003) Nanoscale materials testing under industrially relevant conditions: High-temperature nanoindentation testing. Z Metallkd 94:798-801
7. Xia J, Li CX, Dong H (2003) Hot-stage nano-characterizations of an iron aluminide. Mater Sci Eng A 354:112-120. doi: 10.1016/S0921-5093(02)00902-4
8. Volinsky AA, Moody NR, Gerberich WW (2004) Nanoindentation of Au and Pt/Cu thin films at elevated temperatures. J Mater Res 19:2650-1657. doi: 10.1557/JMR.2004.0331
9. Hinz M, Kleiner A, Hild S, Marti O, Durig, Gotsmann B, Drechsler U, Albrecht TR, Vettiger P (2004) Temperature dependent nano indentation of thin polymer films with the scanning force microscope. Eur Polym J 40:957-964. doi: 10.1016/j.eurpolymj.2004.01.027
10. Schuh CA, Packard CE, Lund AC (2006) Nanoindentation and contact-mode imaging at high temperatures. J Mater Res 21:725-736. doi: 10.1557/JMR.2006.0080
11. Trenkle JC, Packard CE, Schuh CA (2010) Hot nanoindentation in inert environments. Rev Sci Inst 81:073901. doi: 10.1063/1.3436633
12. Franke O, Trenkle JC, Schuh CA (2010) Temperature dependence of the indentation size effect. J Mater Res 25:1225-1229. doi: 10.1557/JMR.2010.0159
13. Rajulapati KV, Biener MM, Biener J, Hodge AM (2010) Temperature dependence of the plastic flow behavior of tantalum. Philos Mag Lett 90:35-42. doi: 10.1080/09500830903356893

14. Suzuki T, Ohmura T (1996) Ultra-microindentation of silicon at elevated temperatures. Philos Mag A 74:1073-1084. doi: 10.1080/01418619608239708
15. Syed-Asif SA, Pethica JB (1997) Nanoindentation creep of single-crystal tungsten and gallium arsenide. Philos Mag A 76:1105-1118. doi: 10.1080/01418619708214217
16. Lund AC, Hodge AM, Schuh CA (2004) Incipient plasticity during nanoindentation at elevated temperatures. App. Phys Lett 85:1362-1364. doi: 10.1063/1.1784891
17. Nieh TG, Iwamoto C, Ikuhara Y, Lee KW, Chung YW (2004) Comparative studies of crystallization of a bulk Zr–Al–Ti–Cu–Ni amorphous alloy. Intermetallics 12:1183-1189. doi: 10.1016/j.intermet.2004.04.011
18. Schuh CA, Mason JK, Lund AC (2005) Quantitative insight into dislocation nucleation from high temperature nanoindentation experiments. Nat Mater 4:617-621. doi: 10.1038/nmat1429
19. Packard CE, Schroers J, Schuh CA (2006) In situ measurements of surface tension-driven shape recovery in metallic glass. Scr Mater 60:1145. doi: 10.1016/j.scriptamat.2009.02.056
20. Sawant A, Tin S (2008) High temperature nanoindentation of a Re-bearing single crystal Ni-base superalloy. Scr Mater 58:275-278. doi: 10.1016/j.scriptamat.2007.10.013
21. Trelewicz JR, Schuh CA (2009) Hot nanoindentation of nanocrystalline Ni-W alloys. Scr Mater 61:1056-1059. doi: 10.1016/j.scriptamat.2009.08.026
22. Bahr DF, Wilson DE, Crowson DA (1999) Energy considerations regarding yield points during indentation. J Mater Res 14:2269-2275. doi: 10.1557/JMR.1999.0303
23. Schuh CA, Lund AC (2004) Application of nucleation theory to the rate dependence of incipient plasticity during nanoindentation. J Mater Res 19:2152-2158. doi: 10.1557/JMR.2004.0276
24. Mason JK, Lund AC, Schuh CA (2006) Determining the activation energy and volume for the onset of plasticity during nanoindentation. Phys Rev B 73:054102. doi: 10.1103/PhysRevB.73.054102
25. Schuh CA, Lund AC, Nieh TG (2004) New regime of homogeneous flow in the deformation map of metallic glasses: Elevated temperature nanoindentation experiments and mechanistic modeling. Acta Mater 52:5879-5891. doi: 10.1016/j.actamat.2004.09.005
26. Packard CE, Schuh CA (2007) Initiation of shear bands near a stress concentration in metallic glass. Acta Mater 55:5348-5358. doi: 10.1016/j.actamat.2007.05.054

27. Jang JI, Lance MJ, Wen SQ, Tsui TY, Pharr GM (2005) Indentation-induced phase transformation in silicon: influences of load, rate and indenter angle on the transformation behavior. Acta Mater 53:1759-1770. doi: 10.1016/j.actamat.2004.12.025
28. Ma XG, Komvopoulos K (2005) In situ transmission electron microscopy and nanoindentation studies of phase transformation and pseudoelasticity of shape-memory titanium-nickel films. J Mater Res 20:1808-1813. doi : 10.1557/JMR.2005.0026
29. Zhang YJ, Cheng YT, Grummon DS (2005) Indentation stress dependence of the temperature range of microscopic superelastic behavior of nickel-titanium thin films. J Appl Phys 98:033505. doi: 10.1063/1.1994934
30. McCormack M, Graebner JE, Tiefel TH, Kammlott GW (1994) Low-temperature thinning of thick chemically vapor-deposited diamond films with a molten Ce-Ni alloy. Diamond related Mater 3:254-258. doi: 10.1016/0925-9635(94)90088-4
31. Everitt NM, Davies MI, Smith JF (2011) High temperature nanoindenation - the importance of isothermal contact. Philos Mag 91:1221-1244. doi: 10.1080/14786435.2010.496745
32. Bei H, George EP, Hay JL, Pharr GM (2005) Influence of indenter tip geometry on elastic deformation during nanoindenation. Phys Rev Lett 95:045501. doi: 10.1103/PhysRevLett.95.045501
33. Ma D, Ong CW, Wong SF, He J (2005) New method for determining Young’s modulus by non-ideally sharp indentation. J Mater Res 20:1498-1506. doi: 10.1557/JMR.2005.0193
34. Perriot A, Vandembroucq D, Barthel E (2006) Raman microspectroscopic characterization of amorphous silica plastic behavior. J Am Ceram Soc 89:596-601. doi: 10.1111/j.1551-2916.2005.00747.x
35. Carreker Jr RP, Hibbard Jr WR (1953) Tensile deformation of high-purity copper as a function of temperature, strain rate, and grain size. Acta Metall 1:654-663
36. Fischer-Cripps AC (2003) Elastic recovery and reloading of hardness impressions with a conical indenter. Mat Res Soc Symp Proc 750:513-518
37. Tabor D (1951) The Hardness of Metals. Clarendon press. Oxford
38. CORNING. Technical Data Sheet. New York. http://www.technicalproductsinc.com/pdf/macor.pdf
39. Leyens C, Peters M (2003) Titanium and Titanium Alloys: Fundamentals and Applications. WILEY-VCH. Weinheim

40. Lütjering G, Williams JG (2007) Titanium. Springer. Berlin
41. Szuecs F, Werner M, Sussmann RS, Pickles CSJ, Fecht HJ (1999) Temperature dependence of Young's modulus and degradation of chemical vapor deposited diamond. J Appl Phys 86:6010-6017. doi: 10.1063/1.371648
42. Carderelli F (2008) Materials Handbook: A Concise Desktop Reference. Springer. New York
43. Heraeus Quarzglas. Base Materials. Technical Properties Sheet. http://heraeus-quarzglas.de/media/webmedia_local/downloads/broschrenbm/BaseMaterials_Image_EN.PDF
44. Meyers MA, Chawla KK (1999) Mechanical behaviors of materials. Prentice-Hall. New Jersey
45. Incropera FP, Dewitt DP (1996) Fundamentals of Heat and Mass Transfer. Willey. New York
46. Durst K, Backes B, Göken M (2005) Indentation size effect in metallic materials: Correcting for the size of the plastic zone. Scr Mater 52:1093-1097. doi: 10.1016/j.scriptamat.2005.02.009
47. Farrissey LM, Mchugh PE (2005) Determination of elastic and plastic material properties using indentation: Development of method and application to a thin surface coating. Mater Sci Eng A 399:254-266. doi: 10.1016/j.msea.2005.03.109
48. Chicot D (2009) Hardness length-scale factor to model nano- and micro-indentation size effect. Mater Sci Eng A 499:454-461. doi: 10.1016/j.msea.2008.09.040
49. Yang FZ, Wornyo E, Gall K, King WP (2008) Thermomechanical formation and recovery of nanoindents in a shape memory polymer studied using a heated tip. Scanning 30:197-202. doi: 10.1002/sca.20074
50. Zhaoyang Y, Xianping L (2010) A preliminary study of micro heat conduction by hot-tip tribological probe microscope. Key Eng Mat 437:374-378. doi: 10.4028/www.scientific.net/KEM.437.374
51. Korte S, Stearn RJ, Wheeler JM, Clegg WJ (2012) High temperature microcompression and nanoindentation in vacuum. J Mater Res 27:167-176. doi: 10.1557/jmr.2011.268

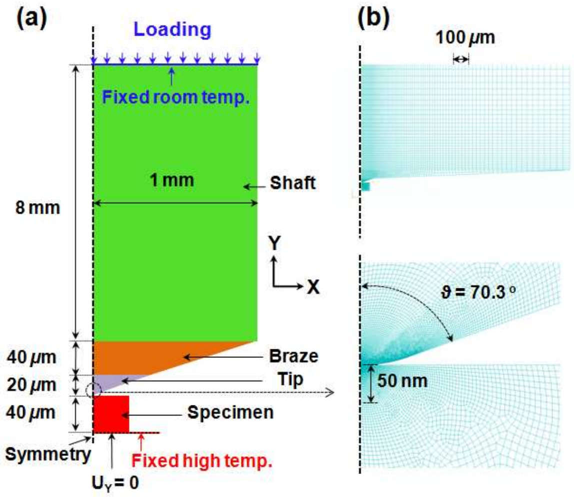

(a)
Loading
Fixed room temp.
1 mm
Shaft
8 mm
Y
X
40 μm
Braze
20 μm
Tip
40 μm
Specimen
Symmetry
Fixed high temp.
$U_Y = 0$
(b)
100 μm
$\vartheta = 70.3°$
50 nm

FIG. 1 (Color online) (a) Schematics of the nanoindentation system including the specimen, indenter tip and the shaft that are joined together by braze alloy, as well as their dimensions. (b) Close-up views of the fine mesh near the contact region and the geometry of the indenter tip.

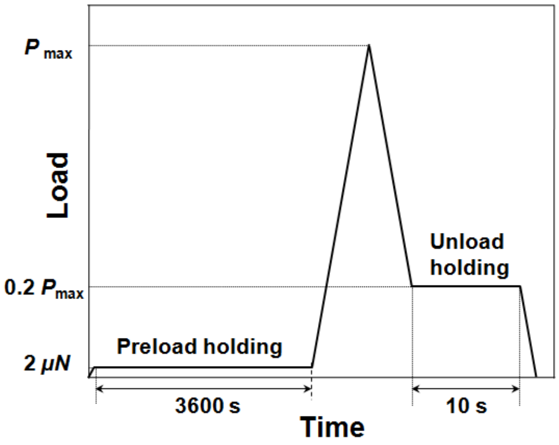
P max
Load
0.2 *P*max
2 *μN*
Preload holding
Unload holding
3600 s
10 s
Time

FIG. 2 Load function used in this study. The loading history includes a preload holding at 2 μN for 3600 s and a unload holding at 20% of the peak load for 10 s.

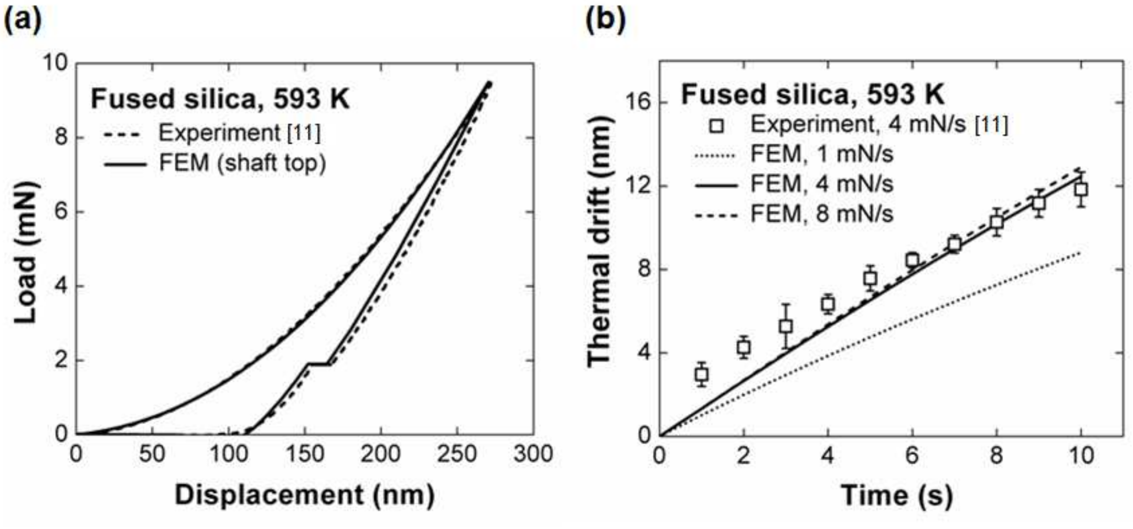

FIG. 3 (a) Comparison between the load-displacement curves obtained from experimental and modeled indentation on fused silica at a set temperature of 593 K using a loading rate of 4 mN/s. Displacements from modeling are those at the top of the shaft. (b) Thermal drift as a function of time extracted from (a), as well as additional results from modeled indentation at 1 mN/s and 8 mN/s.

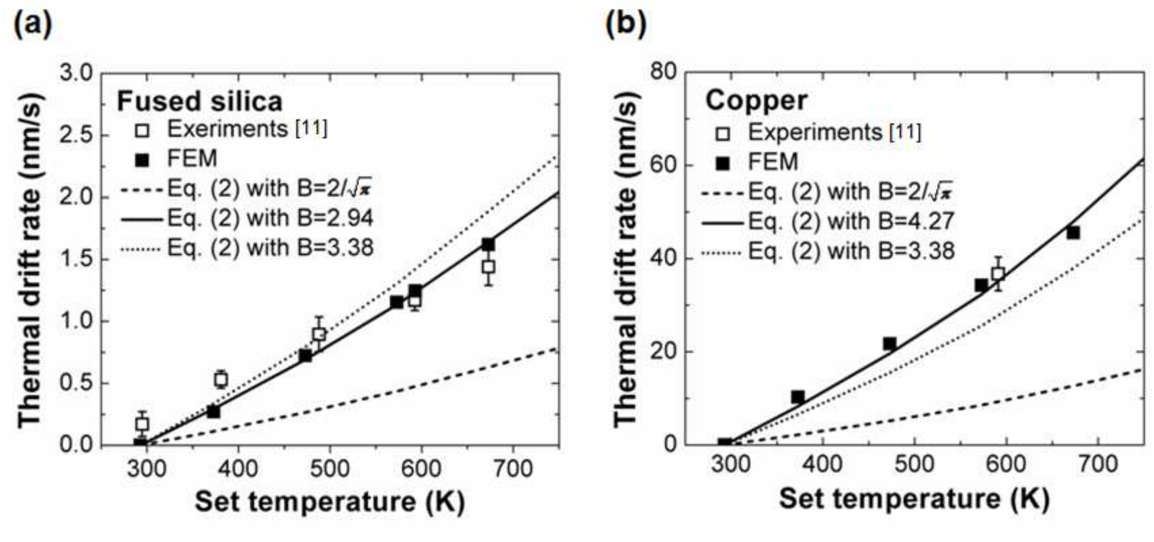

FIG. 4 Thermal drift rate as a function of specimen temperature from FEM (filled symbols) and experiments (open symbols) at a rate of 4 mN/s for (a) fused silica and (b) copper. The lines in each figure are the predictions of Equation (2) with different values of constant *B*.

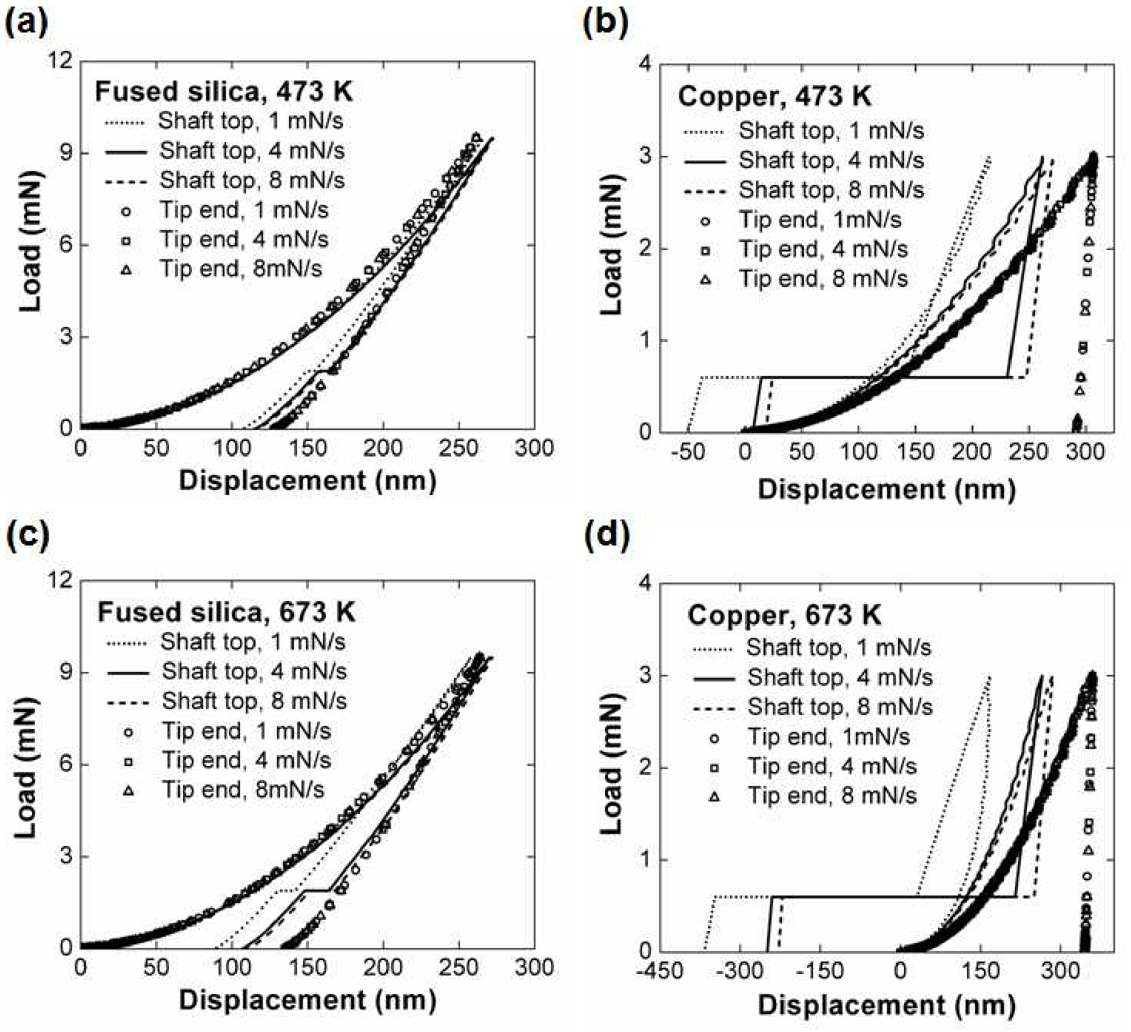

FIG. 5 Load – displacement curves at three different rates from FEM for the case of (a) fused silica at a set temperature of 473 K, (b) copper at a set temperature of 473 K, (c) fused silica at a set temperature of 673 K and (d) copper at a set temperature of 673 K.

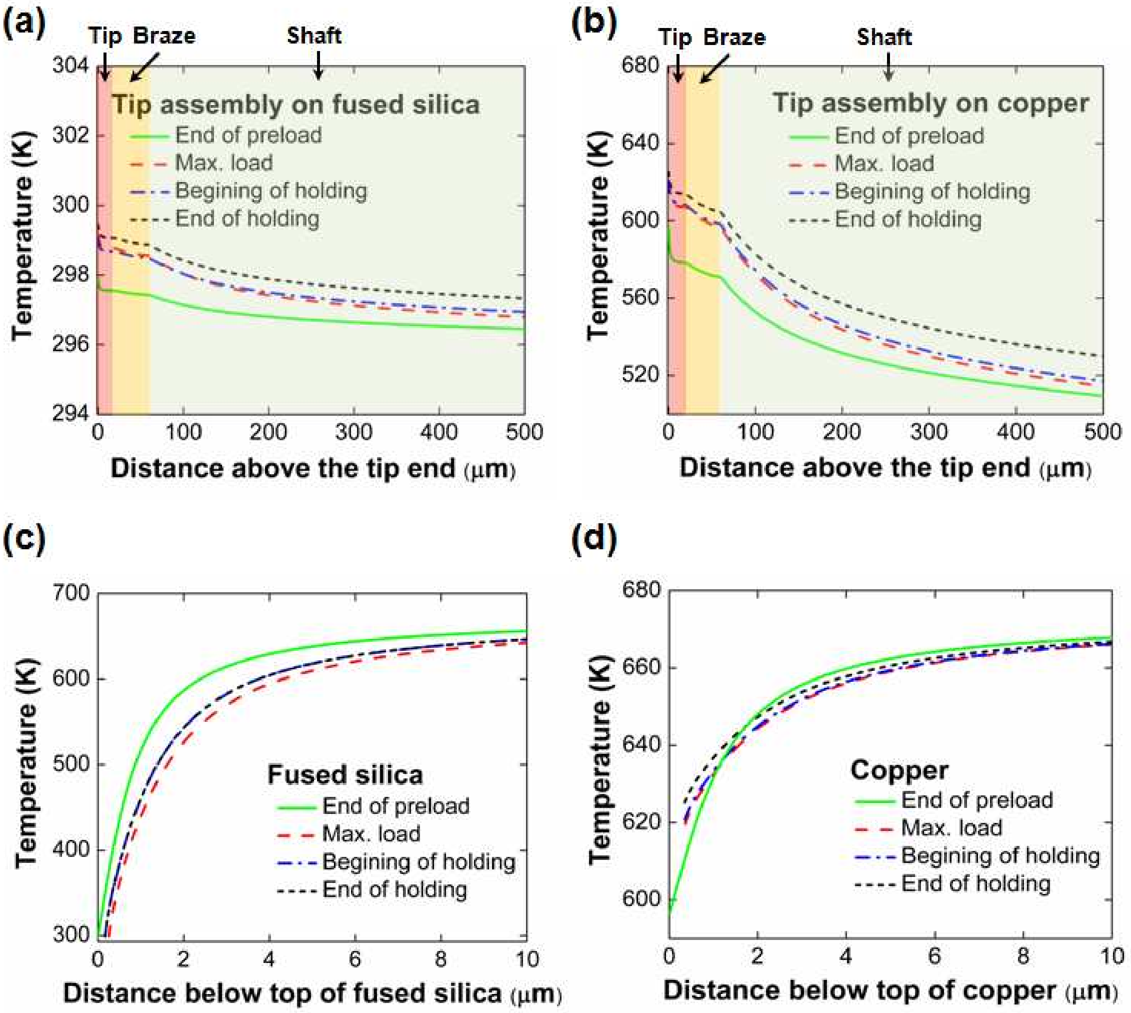

FIG. 6 (Color online) Temperature distribution along the axisymmetric axis (i.e., x = 0 above and below the center of contact) in both the tip assembly (the three different colored zones represent the tip, braze and shaft respectively) and the specimen at a set temperature of 673 K. The loading rate used is 4 mN/s in all cases.

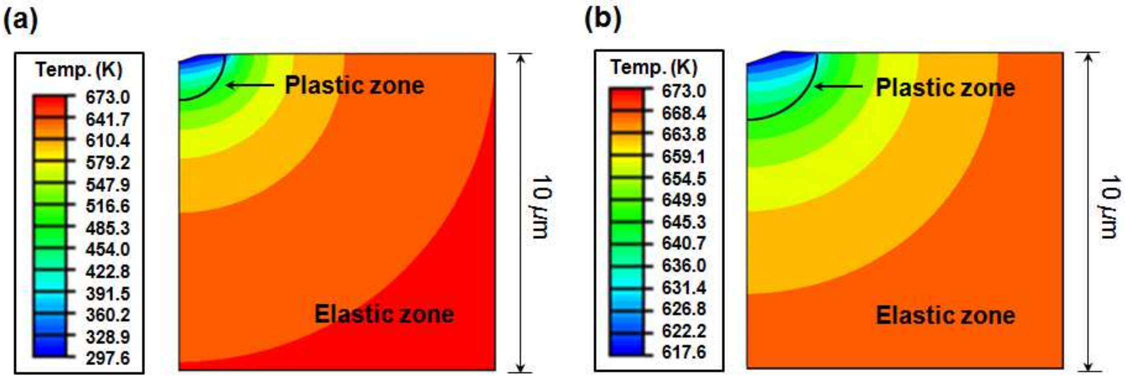

FIG. 7 (Color online) Contour plots of temperature in (a) fused silica at the peak load of 9.5 mN and (b) copper at the peak load of 3 mN right beneath and around contact. The initial specimen temperature is set to be at 673 K for both, and both indentations are carried out at a rate of 4 mN/s.

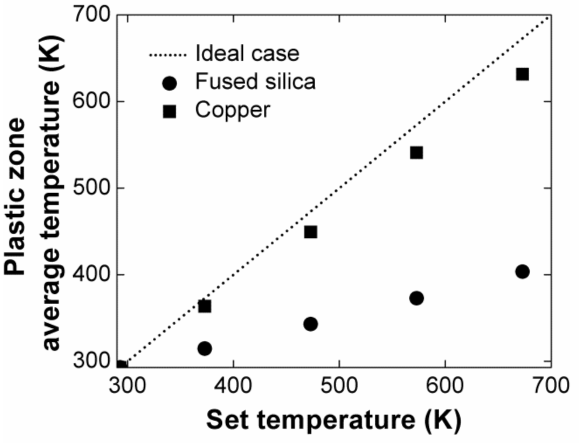

FIG. 8 Comparison between average plastic zone temperature at the peak load with the set temperature for fused silica and copper; all data points are acquired at a loading rate of 4 mN/s

TABLE 1 Materials properties used in this study.

Materials	Macor (Shaft)	Titanium (Braze)	Diamond (Tip)	Fused silica (Specimen 1)	Pure copper (Specimen 2)
Elastic modulus (GPa)	66.9 [38]	115 [39]	$1140[1-1.03\times 10^{-4}(T-293)]$[41]	$75.93-3.94\times e^{[-(T-273)/136.23]}$ [11]	$129.42-5.34\times 10^{-2}T$ [11]
Poisson's ratio	0.29 [38]	0.33 [39]	0.07 [42]	0.17 [43]	0.33 [44]
Yield stress (GPa)	X	X	X	$[9.25-2.81\times 10^{-3}(T-273)]/1.5$ [11]	$[1.03-9.53\times 10^{-4}(T-273)]/3$ [11]
Thermal conductivity (W/mK)	1.46 [38]	20 [40]	2400 [30]	$0.97+1.26\times 10^{-3}T$ [43]	$420.71-6.89\times 10^{-2}T$ [45]
Density (g/cm^3)	2.52 [38]	4.50 [40]	3.51[42]	2.2 [43]	8.96 [42]
Thermal expansion coefficient (1/K)	9.3×10^{-6} [38]	8.4×10^{-6} [40]	1.2×10^{-6} [42]	5.5×10^{-7} [43]	16.5×10^{-6} [42]
Specific heat capacity (J/kgK)	790 [38]	523[40]	509 [42]	772 [43]	385 [42]
F value (MPa)	X	X	X	0	$1139.15-1.31T$ [35]
n value	X	X	X	X	$0.62-2.21\times 10^{-4}\ T$ [35]

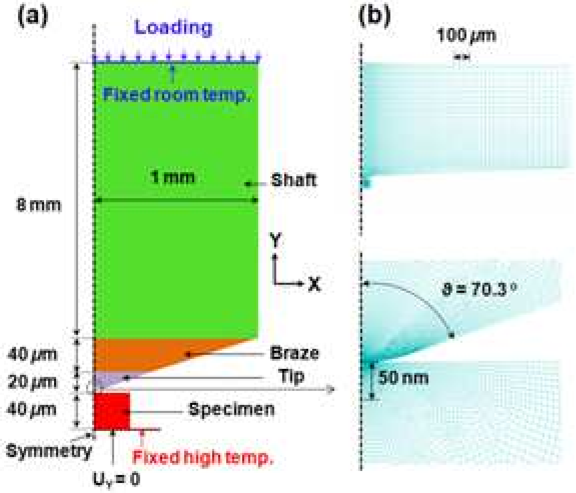
(a)
Loading
Fixed room temp.
8 mm
1 mm
Shaft
Y
X
40 μm
Braze
20 μm
Tip
40 μm
Specimen
Symmetry
Fixed high temp.
U_Y = 0
(b)
100 μm
θ = 70.3°
50 nm

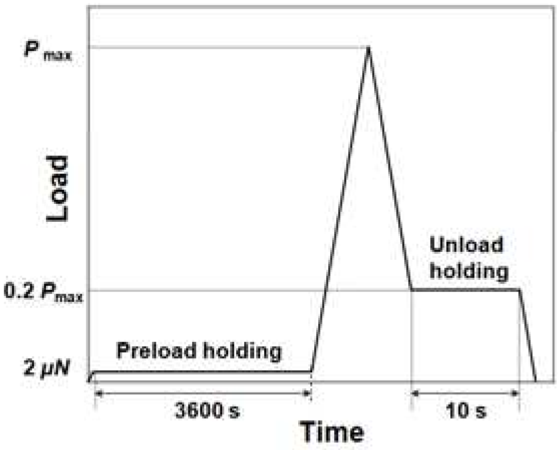
P max
Load
Unload holding
0.2 P max
Preload holding
2 μN
3600 s
Time
10 s

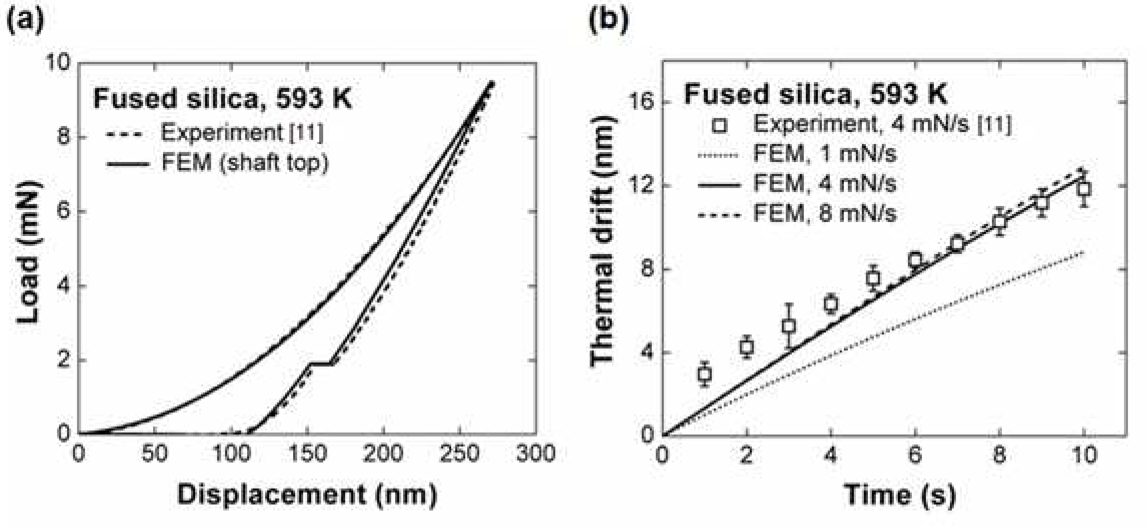
(a)
Fused silica, 593 K
Experiment [11]
FEM (shaft top)
Load (mN)
0
2
4
6
8
10
Displacement (nm)
0
50
100
150
200
250
300
(b)
Fused silica, 593 K
Experiment, 4 mN/s [11]
FEM, 1 mN/s
FEM, 4 mN/s
FEM, 8 mN/s
Thermal drift (nm)
0
4
8
12
16
Time (s)
0
2
4
6
8
10

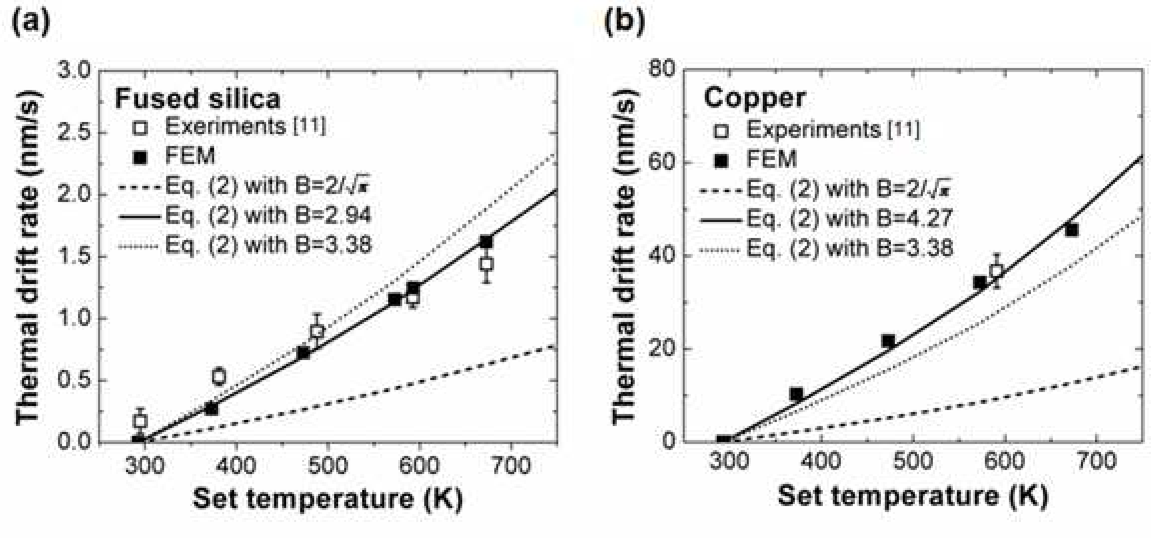
(a)
Fused silica
Exeriments [11]
FEM
Eq. (2) with B=2/√π
Eq. (2) with B=2.94
Eq. (2) with B=3.38
Thermal drift rate (nm/s)
0.0
0.5
1.0
1.5
2.0
2.5
3.0
Set temperature (K)
300
400
500
600
700
(b)
Copper
Experiments [11]
FEM
Eq. (2) with B=2/√π
Eq. (2) with B=4.27
Eq. (2) with B=3.38
Thermal drift rate (nm/s)
0
20
40
60
80
Set temperature (K)
300
400
500
600
700

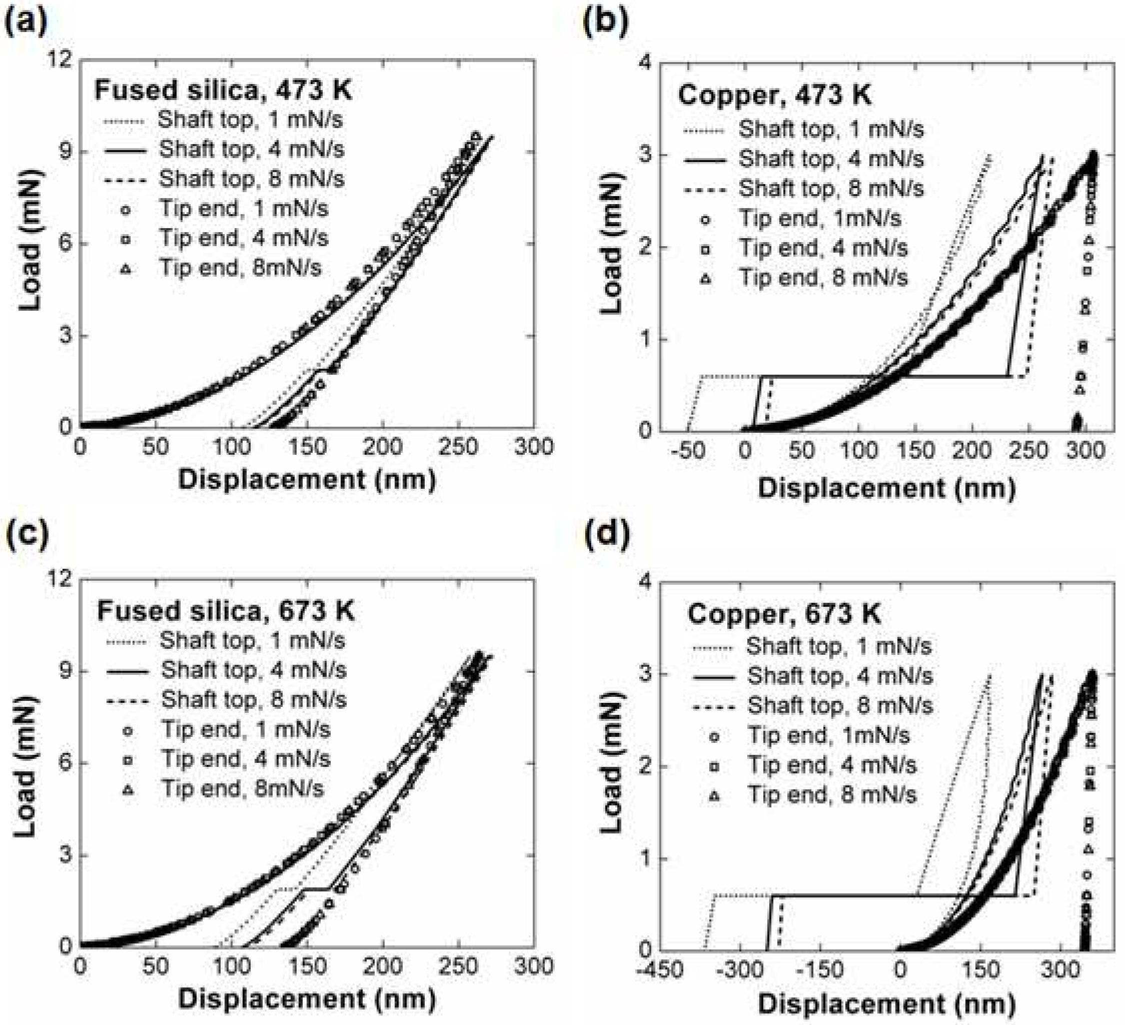

(a)
Fused silica, 473 K
Shaft top, 1 mN/s
Shaft top, 4 mN/s
Shaft top, 8 mN/s
Tip end, 1 mN/s
Tip end, 4 mN/s
Tip end, 8mN/s
Load (mN)
Displacement (nm)
0
3
6
9
12
0
50
100
150
200
250
300
(b)
Copper, 473 K
Shaft top, 1 mN/s
Shaft top, 4 mN/s
Shaft top, 8 mN/s
Tip end, 1mN/s
Tip end, 4 mN/s
Tip end, 8 mN/s
Load (mN)
Displacement (nm)
0
1
2
3
4
-50
0
50
100
150
200
250
300
(c)
Fused silica, 673 K
Shaft top, 1 mN/s
Shaft top, 4 mN/s
Shaft top, 8 mN/s
Tip end, 1 mN/s
Tip end, 4 mN/s
Tip end, 8mN/s
Load (mN)
Displacement (nm)
0
3
6
9
12
0
50
100
150
200
250
300
(d)
Copper, 673 K
Shaft top, 1 mN/s
Shaft top, 4 mN/s
Shaft top, 8 mN/s
Tip end, 1mN/s
Tip end, 4 mN/s
Tip end, 8 mN/s
Load (mN)
Displacement (nm)
0
1
2
3
4
-450
-300
-150
0
150
300

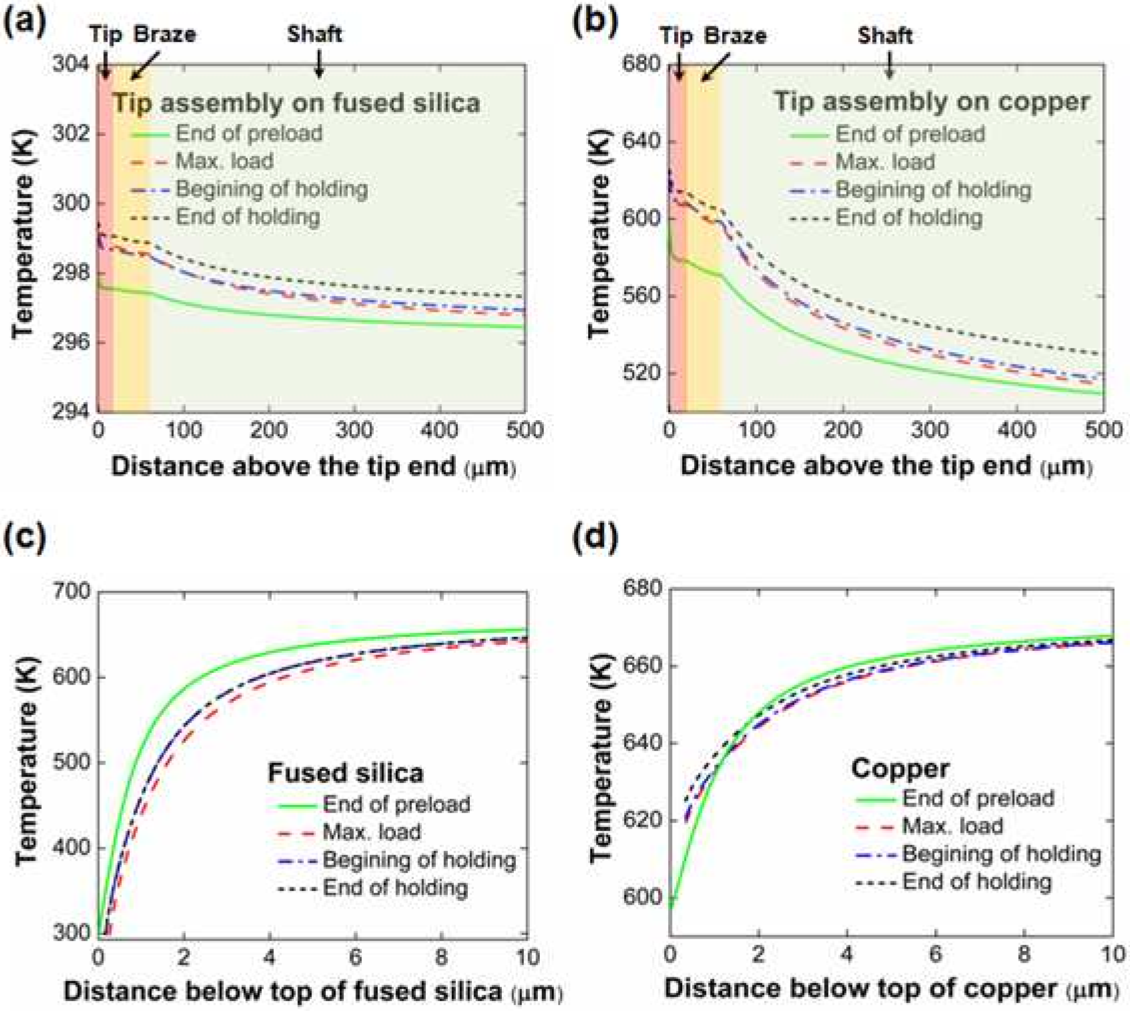
(a)
Tip
Braze
Shaft
Tip assembly on fused silica
End of preload
Max. load
Begining of holding
End of holding
Temperature (K)
304
302
300
298
296
294
0
100
200
300
400
500
Distance above the tip end (μm)
(b)
Tip
Braze
Shaft
Tip assembly on copper
End of preload
Max. load
Begining of holding
End of holding
Temperature (K)
680
640
600
560
520
0
100
200
300
400
500
Distance above the tip end (μm)
(c)
Fused silica
End of preload
Max. load
Begining of holding
End of holding
Temperature (K)
700
600
500
400
300
0
2
4
6
8
10
Distance below top of fused silica (μm)
(d)
Copper
End of preload
Max. load
Begining of holding
End of holding
Temperature (K)
680
660
640
620
600
0
2
4
6
8
10
Distance below top of copper (μm)

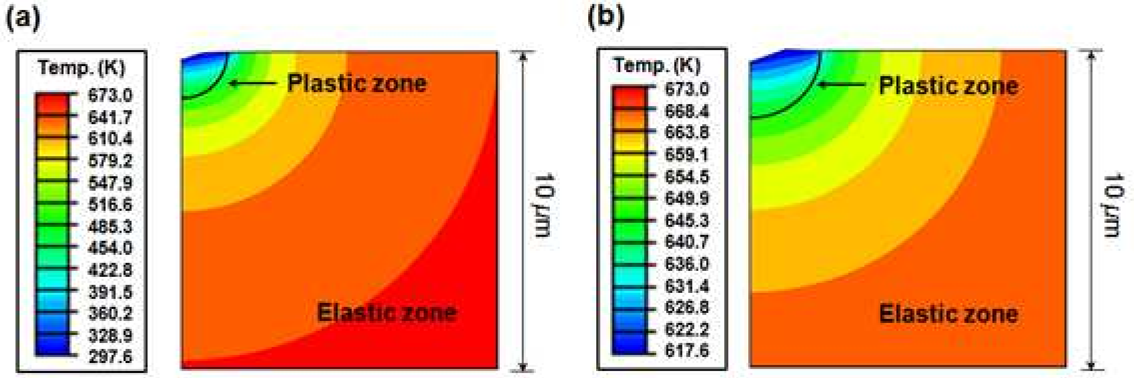
(a)
Temp. (K)
673.0
641.7
610.4
579.2
547.9
516.6
485.3
454.0
422.8
391.5
360.2
328.9
297.6
Plastic zone
Elastic zone
10 μm
(b)
Temp. (K)
673.0
668.4
663.8
659.1
654.5
649.9
645.3
640.7
636.0
631.4
626.8
622.2
617.6
Plastic zone
Elastic zone
10 μm

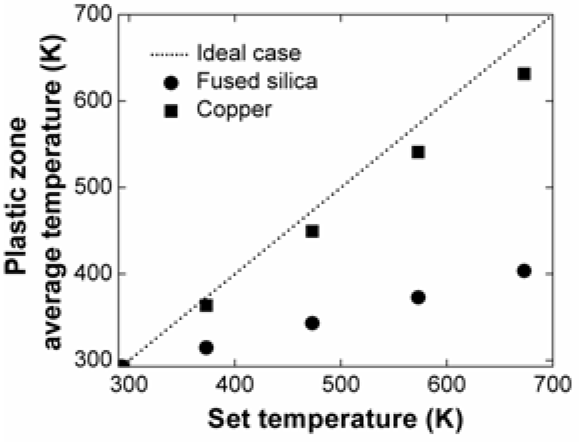
Plastic zone
average temperature (K)
700
600
500
400
300
Set temperature (K)
300
400
500
600
700
Ideal case
● Fused silica
■ Copper